

CoCrFeNiSi high entropy alloy: Synthesis, structural and radiation shielding properties

Hakan Yaykaşlı^a, Hasan Eskalen^{b,*}, Yusuf Kavun^c, Musa Gögebakan^d, Ahmet Hulusi Kaya^e, Nuri Yorulmaz^f

^a Kahramanmaraş İstiklal University, Elbistan Vocational School of Higher Education, Kahramanmaraş, Turkey

^b Kahramanmaraş Sütçü İmam University, Department of Opticianry, Vocational School of Health Services, Kahramanmaraş, Turkey

^c Kahramanmaraş Sütçü İmam University, Department of Medical Imaging Techniques, Vocational School of Health Services, Kahramanmaraş, Turkey

^d Kahramanmaraş Sütçü İmam University, Department of Physics, Kahramanmaraş, Turkey

^e Kahramanmaraş Sütçü İmam University, Department of Materials Sciences and Engineering, Kahramanmaraş, Turkey

^f Faculty of Arts and Sciences, Department of Physics, Harran University, Sanliurfa, Turkey



ARTICLE INFO

Keywords:

High entropy alloy
Radiation shielding
XRD
CoCrFeNiSi

ABSTRACT

High entropy alloys (HEAs) have emerged as a distinct class of alloys with unique design strategies, different from traditional alloys. These alloys hold great promise for diverse applications, and the investigation of their nuclear radiation shielding properties has become an important and emerging area of research. In this experimental study, an equimolar CoCrFeNiSi HEA was prepared using the ball milling method. The focus was on characterizing the crystalline structure, morphological features, and radiation shielding properties of the synthesized HEA. X-ray diffraction analysis revealed that the HEA exhibited a face-centered cubic (FCC) phase structure. The crystallite size was significantly reduced from 23.63 nm to 3.22 nm, indicating the refinement of the microstructure. The homogeneity of the alloy was confirmed through scanning electron microscopy with energy-dispersive X-ray spectroscopy (SEM-EDX), which showed that the five elements were uniformly distributed within the powder alloy. To evaluate the radiation shielding properties, linear attenuation coefficients (LAC) of the CoCrFeNiSi HEA powder were measured using a 662 keV gamma source and a NaI(Tl) detector system (ORTEC® 905-4). The experimental LAC values were determined to be $0.2140 \pm 0.01 \text{ cm}^{-1}$. Theoretical calculations using MCNP6.2 and XCOM code were also performed and showed good agreement with the experimental results. Comparing the CoCrFeNiSi HEA with common shield materials such as thin films, glass systems, and some composites, it was found that the HEA outperformed them in terms of radiation shielding effectiveness. This demonstrates the potential of the CoCrFeNiSi HEA as an advanced alternative to conventional shielding materials, with potential applications in various fields.

1. Introduction

High entropy alloys (HEAs) represent a new class of materials that have garnered increasing attention from researchers. They have attracted attention due to their outstanding properties, such as good thermal stability, high strength, corrosion resistance, high hardness, catalytic properties, and excellent wear performance (Addepalli et al., 2022; Ashwini et al., 2022; Shkodich et al., 2022). The designation of an alloy as a high-entropy alloy requires two essential properties: (a) the alloy must consist of five or more elements, and (b) the atomic percentage of each element in the alloy must be greater than 5% and less than 35% (Hu

et al., 2022; Nagarjuna et al., 2022; Zhang et al., 2022). HEAs can be synthesized using various methods, including electrochemical deposition, de-alloying, arc melting, laser cladding, and mechanical alloying (Kumar et al., 2022a). The latter-mentioned methods are one of the most popular methods for producing HEAs (Toroghinejad et al., 2022a). By using this method, various kinds of homogenous materials can be synthesized at room temperature without segregation and inhomogeneous products (Shkodich et al., 2022).

Today, researchers have been focused on the development of radiation shielding materials. Radiation protection by shielding is essential when using distance and time is not feasible (Kaewjaeng et al., 2021).

* Corresponding author.

E-mail addresses: eskalen@ksu.edu.tr, heskalen@gmail.com (H. Eskalen).

Table 1

Characteristic properties of the elements (Miedema et al., 1980; Taghvaei and Khoshrodi, 2018).

Element	Crystal Structure	Atomic Radius (Å)	Melting Point (K)	Density (g/cm³)
Cobalt	HCP	1.26	1768	8.90
Chromium	BCC	1.27	2130	7.19
Iron	BCC	1.25	1808	7.86
Nickel	FCC	1.21	1726	8.90
Silicon	DC	1.11	1683	2.33

HCP: hexagonal close packed, BCC: body-centered cubic, FCC: face-centered cubic, DC: diamond cubic.

Since it is evident that there is a significant increase in ionizing radiation sources in different applications. Various types of materials have been considered for this, including thin films (Eskalen et al., 2020; Kavun et al., 2022), polymer composites (Kavun et al., 2021), glasses (Alfryyan et al., 2022; Cheewasukhanont et al., 2022; Kavun et al., 2021) and alloys (Yaykaşlı et al., 2022). Lead (Pb) has known as conventional materials for radiation shielding because of this high density and large atomic number but it has weak points in terms of rigidity, toxicity and weight (Wang et al., 2021). Because of these mentioned shortcomings lead-free materials are considered of particular interest (Almurayshid et al., 2021).

The literature extensively explores the radiation shielding properties of certain alloys. Agar et al. conducted a study on the radiation shielding performance of alloys containing palladium (Pd) and silver (Ag). Their research revealed that the Pd75/Ag25 alloy exhibited the most promising photon shielding results (Agar et al., 2019). High-entropy alloys (HEAs) stand out as excellent candidates for advanced nuclear applications due to their unique and exceptional physical, chemical, and thermal properties (Moschetti et al., 2022). Wang et al. synthesized a GaInSnPbBi HEA and demonstrated that it possessed a higher mass attenuation coefficient than even lead (Wang et al., 2021). Another recent study focused on the nuclear shielding properties of HEAs, highlighting the excellent gamma-ray shielding characteristics of the NiCoFeCrW alloy compared to the control samples (Gul et al., 2022). This work aims to investigate the structural, morphological, and ionizing radiation attenuation characteristics of a newly fabricated Co₂₀Cr₂₀Fe₂₀Ni₂₀Si₂₀ high-entropy alloy as its primary objective.

2. Material method

Cobalt, chromium, iron, nickel and silicon (purity higher than 99.9%) used in the alloying process has been purchased from Alfa Aesar. Alloy was weighted by equiatomic ratio Co₂₀Cr₂₀Fe₂₀Ni₂₀Si₂₀ (at. %) and placed in hardened stainless-steel vials and milling balls of different sizes were utilized. The prepared powders were placed in a high energy

planetary ball mill (Fritsch Pulverisette 5 model) at 300 rpm rotation speed with a ball to powder weight ratio of 20:1. The process was set to run for 20 min and stop for 20 min to inhibited overheating. The total milling process continued for 100 h. Samples were taken at different time intervals (0, 5, 10, 20, 30, 50 and 100 h), and some characterizations were made depending on the grinding time. Some important properties of the initial elements are given in Table 1.

The crystallography analysis of the alloys was carried out using an X-ray diffractometer (Philips X'Pert PRO) with CuK α ($\lambda = 1.54 \text{ \AA}$) radiation 40 kV, 30 mA. The scan was performed in the range $2\theta = 20^\circ - 110^\circ$. The morphological microstructure and chemical composition of powders were observed with scanning electron microscopy (SEM, ZEISS EVO LS10) and X-ray Energy-Dispersive Spectroscopy (EDS) respectively. The Co₂₀Cr₂₀Fe₂₀Ni₂₀Si₂₀ (100 h of milled) alloy powders were prepared to measure radiation transmittance. Green pellets were formed with a fixed diameter of 13 mm and various thicknesses, primarily 1.22, 2.3, 2.9, 3, 3.23, 4.14, and 5 mm. These pellets were utilized for the radiation shielding measurement.

Average crystallite size estimate through modified Scherrer equation (least squares technique), the average crystallite size (D) of alloyed powders as a function of milling times is given as (Prasad et al., 2023),

$$\ln(\beta) = \ln \frac{1}{\cos \theta} + \ln \frac{K\lambda}{D} \quad (1)$$

where K is the shape factor (Scherrer constant) with the value 0.90, $\lambda = 0.15406 \text{ nm}$ (wavelength of X ray sources), β is the full width at half maximum in radians and θ is the peak position (in radians). Since the exact K-value is not known for the present system, D-values are only estimates. The microstrain was determined by using following Equation (Eq. 2) (Goktas et al., 2022; Yaykaşlı, 2023)

$$\varepsilon = \frac{\beta_{hkl}}{4 \tan \theta} \quad (2)$$

Valence electron concentration (VEC) is calculated using Equation (3). The enthalpy of mixing (ΔH_{mix}) for a multi-component alloy was calculated using Equation (4). The entropy of mixing (ΔS_{mix}) of an n-element alloy was calculated using Equation (5). The parameter atomic size difference (δ) was calculated as using Equation (6) (Kumar et al., 2016, 2022b).

$$VEC = \sum_i^n c_i (VEC)_i \quad (3)$$

$$\Delta H_{mix} = \sum_{i=1, j \neq i}^n \Omega_{ij} c_i c_j \quad (4)$$

$$\Delta S_{mix} = -R \sum_{i=1}^n c_i \ln c_i \quad (5)$$

Table 2

The structure, the entropy of mixing (ΔS_{mix}), the enthalpy of mixing (ΔH_{mix}), Valence electron concentration (VEC), the atomic radius difference (δ), and of the CoCrFeNiSi alloy systems (atomic percent).

Alloy	Structure	ΔH_{mix}	ΔS_{mix}	VEC	$\delta(\text{\AA})$	References
CoCrFeNiSi	fcc	-18.16	13.38	7.4	4.87	In this study
CoFeNi	fcc	-1.33	9.13	9.00	0.33	Wang et al. (2012)
CrFeNi	fcc	-4.44	9.13	8.00	0.26	Singh and Subramaniam (2012)
CoFeNiSi _{0.25}	fcc	-	-	8.62	1.98	Zuo et al. (2014)
CoCrFeNi	fcc	-3.75	11.53	8.25	0.30	Liu et al. (2021)
CoCrFeNiMo	fcc	-1.52	13.38	8.25	1.28	Wu et al. (2022)
CoCrFeNiHf	fcc	-	13.38	-	5.352	Ma and Shek (2020)
CoCrFeNiCu	fcc	3.20	13.38	8.80	1.07	Yeh et al. (2004)
CoCrFeNiY _{0.3}	fcc	-6.03	12.82	7.88	10.72	Zhang et al. (2018)
CoCrFeNiNb _{1.0}	fcc	-14.88	-	7.60	6.32	Jiang et al. (2018)
CoCrFeNiCu _{0.5} Si	fcc	-18.48	14.53	8.10	2.15	Chen et al. (2018)
CoCrFeNiAl	fcc + bcc	-12.32	13.38	-	5.77	Ji et al. (2014)
CoCrFeNiCuAl	fcc + bcc	-4.78	14.90	-	5.28	Xu et al. (2019)
CoCrFeNiSi _{0.2} Al _{0.5}	fcc + bcc	-14.1	14.00	7.5	4.9	Zhang et al. (2015)

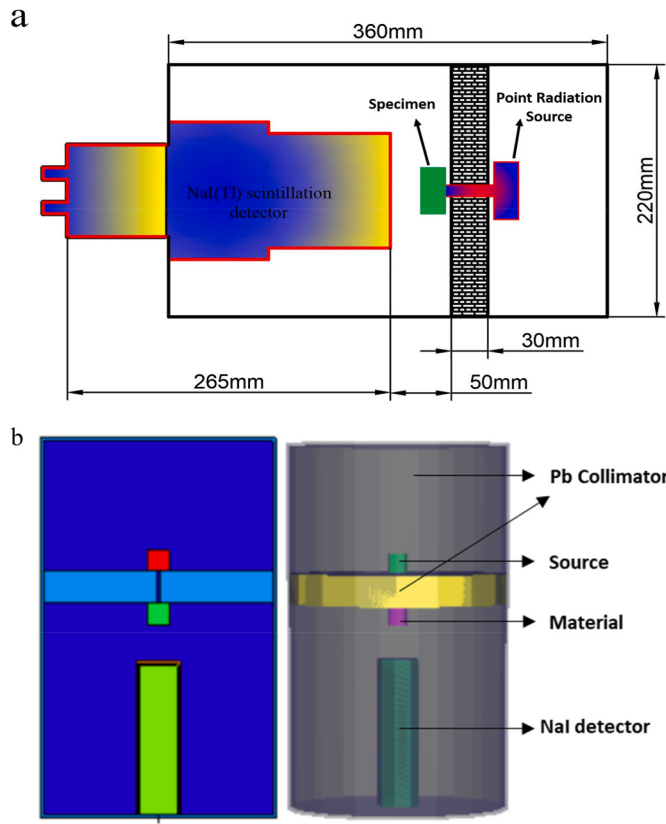


Fig. 1a. Experimental Schema of radiation shielding measurements bMCNP 2D and 3D simulation geometry.

$$\delta = 100 \sqrt{\sum_{i=1}^n c_i \left(1 - \frac{r_i}{\bar{r}}\right)^2} \quad (6)$$

where $\Omega_{ij} = 4\Delta H_{mix}^{AB}$ is defined as the mixing enthalpy of binary A-B alloys in the liquid state, c_i and c_j are atomic percentage of the i_{th} and j_{th} element, respectively, r_i is the atomic radius of the i_{th} element, $\bar{r} = \sum_{i=1}^n c_i r_i$ is the average atomic radius, and R is the gas constant, $8.314 \text{ J K}^{-1}\text{mol}^{-1}$. References used for VEC of elements (GUO and LIU, 2011) and ΔH_{mix}^{AB} the mixing enthalpy of binary A-B alloys (<http://www.entall.imim.pl/calculator/>). Some key characteristics of alloy systems is given in Table 2.

A wide variety of alloy types have formed the basis for many shielding materials to date. Here, gamma-ray shielding properties were investigated by doping various amounts of Si to the $\text{Co}_{20}\text{Cr}_{20}\text{Fe}_{20}\text{Ni}_{20}\text{Si}_{20}$ HEA. The amount of gamma-ray's transmission of a material is determined by the Lambert-Beer law given in Eq. (7);

$$\mu = \ln\left(\frac{I}{I_0}\right) / (-x) (\text{cm}^{-1}) \quad (7)$$

here x is the material thickness, I_0 is the amount of gamma rays that reach the detector without interacting with the material, and I is the amount of gamma rays that reach the detector after interacting material, and μ is the linear attenuation coefficient (LAC). The Lambert-Beer law gives us the radiation permittivity of a material of thickness x (I/I_0). In this equation, μ is given as the linear attenuation coefficient (LAC) (equation (7)). By definition of the Lambert-Beer law, it is a measure of the probability of radiation interacting with atoms in matter per unit length (ALMISNED et al., 2023). By this definition, LAC is independent of material thickness.

The standard deviation corresponding to the absorption of gamma

rays is calculated by Eq. (8). μ values are used in this equation.

$$\sigma = \sqrt{\frac{\sum_{i=1}^N (\mu_i - \bar{\mu})^2}{N - 1}} \quad (8)$$

in Eq. (8), $\bar{\mu}$ represents the mean lac values and N represents the number of measurements for samples.

Mass Attenuation Coefficient (Knoll and Krane, 1981), indicates the amount of gamma absorbed by a unit mass. Eq. (9) shows the formula used to calculate the MAC for a compound and mixture:

$$\mu_m = \frac{\mu}{\rho} = \sum w_i \left(\frac{\mu}{\rho} \right)_i (\text{cm}^2 / \text{g}) \quad (9)$$

here, the mass fraction is w_i , the density is ρ , and the MAC for elements in the compound is $(\frac{\mu}{\rho})_i$.

Material thickness that transmits half of the incoming gamma rays is expressed as Half Value Layer (HVL) (Krane and Lynch, 1989), and material thickness that passes one-tenth of it is expressed as Tenth Value Layer (TVL). These are given in Eqs. (10) and (11), respectively. The term that expresses the path that gamma rays can take in the material is given in Eq. (12) as Mean Free Path (MFP) (Knoll and Krane, 1981).

$$\text{Half Value Layer (HVL)} = \frac{\ln 2}{\mu} (\text{cm}) \quad (10)$$

$$\text{Tenth Value Layer (TVL)} = \frac{\ln 10}{\mu} (\text{cm}) \quad (11)$$

$$\text{Mean Free Path (MFP)} = \frac{1}{\mu} (\text{cm}) \quad (12)$$

with the experimental setup shown in Fig. 1a, measurements were made with the NaI(Tl) (ORTEC® 905-4) detector system using gamma-ray with 662 keV energy obtained from the ^{137}Cs source with 0.25 mCi activity.

MCNP (Monte Carlo N-Particle) is a radiation transport program used by nuclear and radiation physicists and engineers to model radiation transport in various applications such as nuclear reactors, medical imaging devices, radiation therapy, and the effects of nuclear weapons (Acikgoz et al., 2022). MCNP models the interactions and transport of radiation in materials statistically. At the core of MCNP lies the Monte Carlo method, which is a simulation technique that statistically replicates the interactions and transport of radiation. The program uses mathematical algorithms to model radiation interactions in various materials, including energy loss, scattering, absorption, and other physical processes. MCNP is one of the leading radiation simulation programs with the largest cross-section library in the literature. XCOM is a database developed and published by NIST (National Institute of Standards and Technology). The XCOM database provides mass attenuation coefficients of various materials as a function of energy level, material type, and material density. This information can be used to estimate how much a material will attenuate when traversed by photon radiation and to calculate dose distributions. The XCOM database is also utilized in calculating separate MAC values for photoelectric effect, Compton scattering, and pair production interactions (Mahmoud et al., 2019).

In this study, a simulation model was created in the MCNP environment with the exact same dimensions of the experimental setup given in Fig. 1a and b. In general terms, this model; It consists of a radiation source emitting photons with 662 keV energy generated by CELL, VEC, NRM and DIR source cards, a material and a NaI detector measuring the photon flux identified by the F4 tally card. Each simulation was run with 107 particle stories, keeping the simulation error below 0.1%. The first simulation was created only from the source-detector pair and the I_0 photon flux of the radiation source was determined. Then, photon flux I values were determined by placing our

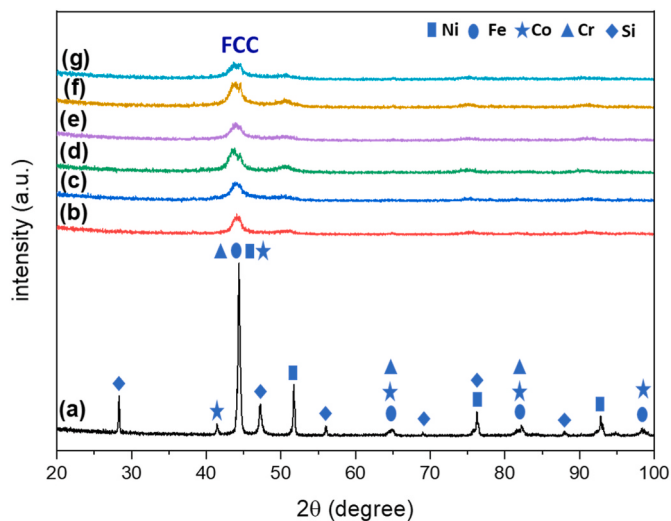


Fig. 2. X-ray diffraction pattern of the $\text{Co}_{20}\text{Cr}_{20}\text{Fe}_{20}\text{Ni}_{20}\text{Si}_{20}$ HEA synthesized by ball milled different times for: (a) 0 h, (b) 5 h, (c) 10 h, (d) 20 h, (e) 30 h, (f) 50 h and (g) 100 h.

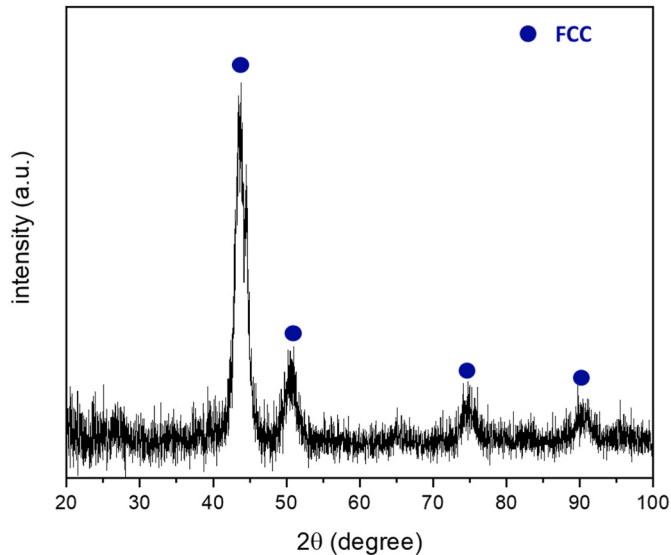


Fig. 3. X-ray diffraction pattern of the $\text{Co}_{20}\text{Cr}_{20}\text{Fe}_{20}\text{Ni}_{20}\text{Si}_{20}$ HEA after 100 h milling.

materials in the relevant thicknesses. In conclusion; LAC values were determined from the thickness graph according to the I/I_0 transition ratio.

3. Results

3.1. Phase analysis of as milled powder

Fig. 2 demonstrates X-Ray diffraction pattern of powder milled CoCrFeNiSi HEA as a function of time. The diffraction peak of the starting sample (0 h, without milling) is basically consist of pure elemental powders. As the milling time is reached to 5 h, the diffraction peaks of Co and Fe disappeared firstly demonstrating that Co and Fe have the highest alloying rate. As the increasing the milling time, more peaks disappear and the intensity of the remaining peaks decreases. The only predominated amorphous phase of powder alloy existed. This situation demonstrates that the metallic powders absorb energy and procedure solid solution structure with each other as function of the

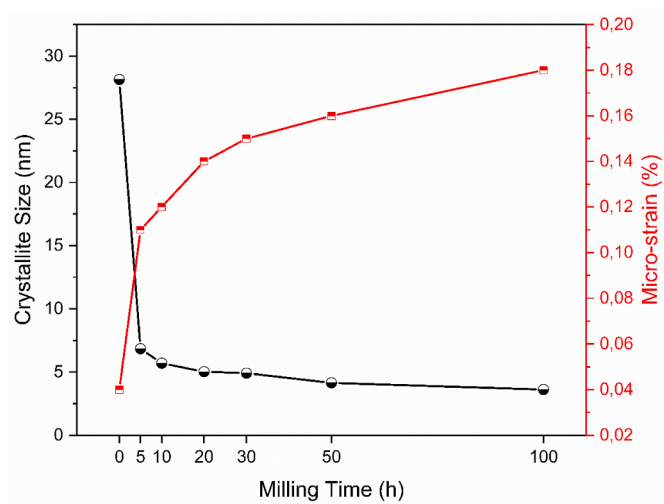


Fig. 4. Crystallite size and micro-strain as a function of milling time.

mechanical milling time (Zhang et al., 2021). Mechanical milling was continued for up to 100 h to observe stability and any phase transformation in the structure. The X-ray diffraction pattern of 100 h ground CoCrFeNiSi HEA powders is shown in Fig. 3. As can be understood from here, it was observed that the phases were stable with 100 h milling only the broadening of the peaks was observed (Shivam et al., 2020). The three primary causes of the peak widening are grain refinement, reduced crystallinity, and increased lattice strain (Liu et al., 2017). There is only one solid solution phase namely face centered cubic (FCC) phase without other intermetallic phase is clearly seen from this graph with diffraction peaks centered around 43.60, 50.53, 74.88 and 90.44 (Güler et al., 2022; Wu et al., 2019).

Using obtained XRD results, structural parameters of the synthesized high entropy alloy such as crystallite size and micro-strain were calculated after 100 h of milling and obtained results shown in Fig. 4. As seen from the figure, crystallite size and micro-strain are an inversely proportional. When the milling time increase, the amount of plastic deformation enhanced this leads to increase in crystal defects and as a result an increase is observed in micro strain values (Toroghinejad et al., 2022). The crystallite size was calculated as 28.15 nm after 1 min ball milling. When milling time reached to 5 h crystallite size decreased to 6.85 nm, finally after 100 h milling the crystallite size calculated as 3.62 nm. The sharp decrease in crystallite size at the initial state of milling process attributed to formation of nanostructured sub-grains resulting from the destruction and recombination of dislocations (Toroghinejad et al., 2022).

3.2. Microstructural characteristics

The morphological characteristics of the $\text{Co}_{20}\text{Cr}_{20}\text{Fe}_{20}\text{Ni}_{20}\text{Si}_{20}$ High Entropy Alloy (HEA) powder obtained were examined in Fig. 5 as a function of milling time. Fig. 5a illustrates the various shapes, sizes, and morphologies of the individual pure elements prior to the milling process. After 5 h of milling, the particles exhibit a rougher texture compared to those at 0 h (Kursun et al., 2018). This roughness is attributed to plastic deformation and the cold-welding process, leading to an increase in particle thickness. Such behavior is a characteristic feature of ductile particles in the early stages of mechanical milling, resulting from the continuous collisions between the powders and balls (García-Garrido et al., 2021). With further milling time, larger particles experience deformation, leading to fragmentation into fragile flakes, as depicted in Fig. 5d. At this period, the amount of aggregated particles getting decreased and the average particle size of powders is reduced (Suryanarayana, 2001). The powders getting spherical shaped geometry

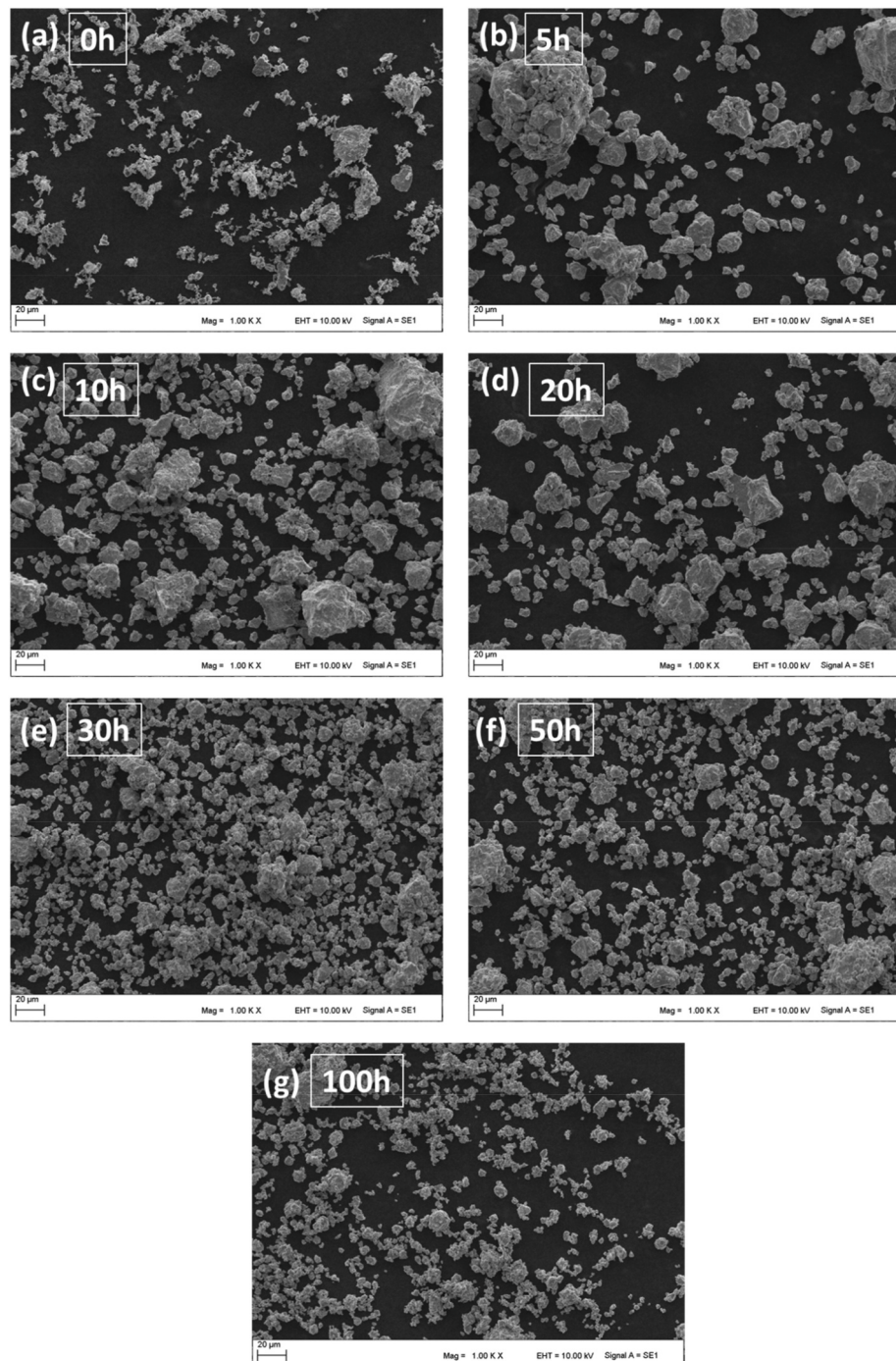


Fig. 5. SEM micrographs of $\text{Co}_{20}\text{Cr}_{20}\text{Fe}_{20}\text{Ni}_{20}\text{Si}_{20}$ HEA powder at different milling times: (a) 0 h, (b) 5 h, (c) 10 h, (d) 20 h, (e) 30 h, (f) 50 h and (g) 100 h.

because of reduction of Gibbs free energy, after 30 h of milling (García-Garrido et al., 2021). The significant morphological changes observed after 100 h of grinding can be summarized as follows: (a) a reduction in the size of large agglomerated particles, (b) a decrease in the particle size of the powders, and (c) a convergence of morphological shapes towards similarity with one another.

The chemical composition of the and its distribution of $\text{Co}_{20}\text{Cr}_{20}\text{Fe}_{20}\text{Ni}_{20}\text{Si}_{20}$ HEA powders after 100 h of milling have been investigated with SEM-EDX maps. The elemental mapping of the powders is illustrated in Fig. 6 (a). This observation supports the high homogeneity and uniform distribution of the obtained $\text{Co}_{20}\text{Cr}_{20}\text{Fe}_{20}\text{Ni}_{20}\text{Si}_{20}$ powder composition. The point EDX analysis of powder after 100 h of mechanical alloying is given in Fig. 6b. The results further indicate a

uniform distribution of all five elements within the powder alloy, affirming the formation of a solid solution with consistent element distribution.

3.3. Radiation shielding study

Estimated Linear Attenuation Coefficient (LAC) of $\text{Co}_{20}\text{Cr}_{20}\text{Fe}_{20}\text{Ni}_{20}\text{Si}_{20}$ HEA powders can be seen in Fig. 7. The permeability values (I/I_0) of $\text{Co}_{20}\text{Cr}_{20}\text{Fe}_{20}\text{Ni}_{20}\text{Si}_{20}$ HEA powders were obtained in the measurements made with the experimental setup in Fig. 1a. In the equation obtained for these I/I_0 ratios seen in Fig. 7, the value of μ was determined as $0.2140 \pm 0.01 \text{ cm}^{-1}$. As it can be understood from here, the LAC value of $\text{Co}_{20}\text{Cr}_{20}\text{Fe}_{20}\text{Ni}_{20}\text{Si}_{20}$ HEA powders is $0.2140 \pm 0.01 \text{ cm}^{-1}$

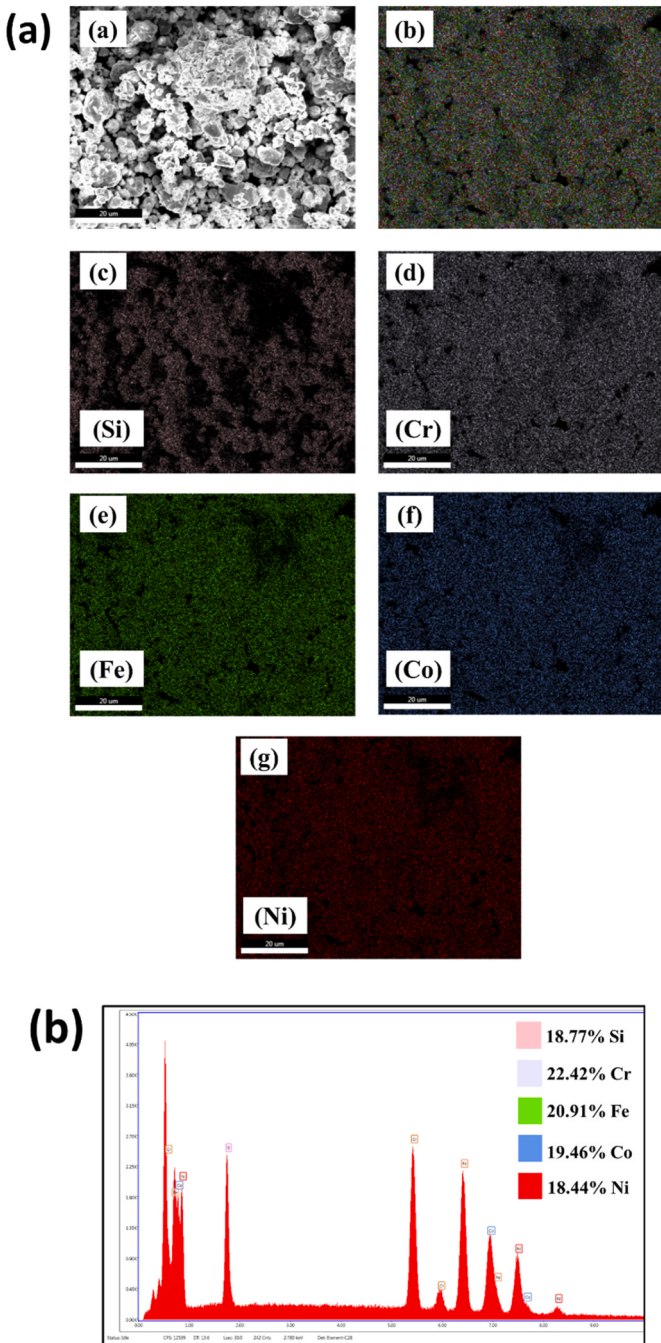


Fig. 6. (a) EDX mapping results of $\text{Co}_{20}\text{Cr}_{20}\text{Fe}_{20}\text{Ni}_{20}\text{Si}_{20}$ HEA powders for 100 h MA times, (b) Elemental composition of powder after 100 h of alloying.

and with the help of this experimentally determined μ value, MAC, HVL, TVL and MFP values were calculated. Similarly, the μ value calculated by creating the experimental system in Fig. 1 in the MCNP6.2 code was determined as 0.23 cm^{-1} .

In the B-doped ZnO coated thin films have been irradiated via 6 MeV energized electrons in the literature, when the B ratio changed between 0% and 15%, the LAC value obtained as $0.0078 \pm 0.001 \text{ cm}^{-1}$ and $0.0125 \pm 0.0012 \text{ cm}^{-1}$ (H. Eskalen et al., 2020). In another thin films irradiated via 6 MeV energized electrons, the ratio of Sm in Sm-doped In_2O_3 coated thin films varied between 0% and 20% and the LAC value increased from $0.00377 \pm 0.000506 \text{ cm}^{-1}$ to $0.00558 \pm 0.000398 \text{ cm}^{-1}$. The radiation shielding properties of graphitic carbon nitride, the thiourea ratio ranged from 0% to 100%, and accordingly, the

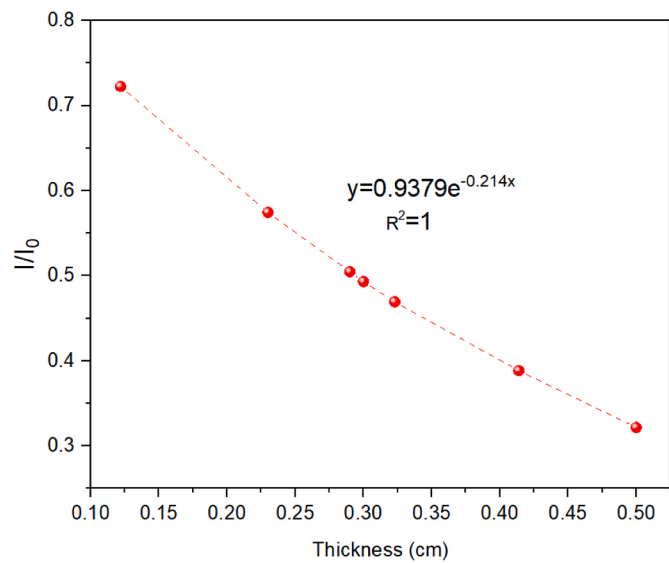


Fig. 7. Estimated Linear Attenuation Coefficient of $\text{Co}_{20}\text{Cr}_{20}\text{Fe}_{20}\text{Ni}_{20}\text{Si}_{20}$ HEA powders at 662 keV gamma energy.

LAC values obtained as $0.0212 \pm 0.0011 \text{ cm}^{-1}$ and $0.1696 \pm 0.0085 \text{ cm}^{-1}$ using 835 keV gammas (Kavun et al., 2023). In the study by Khanna A. et al., The Linear Attenuation Coefficient values of some heavy metal glasses values were obtained between 0.291 cm^{-1} and 0.529 cm^{-1} at 662 keV gamma energy (Khanna et al., 1996).

Also, the Mass Attenuation Coefficient (MAC) of $\text{Co}_{20}\text{Cr}_{20}\text{Fe}_{20}\text{Ni}_{20}\text{Si}_{20}$ HEA powders at 662 keV gamma energy have been calculated using the obtained LAC values. Accordingly, the experimentally obtained MAC value was calculated as $0.0648 \text{ cm}^2/\text{g}$. The MAC value obtained with the MCNP6.2 code was calculated as $0.0696 \text{ cm}^2/\text{g}$. The MAC value obtained with XCOM was determined as $0.0740 \text{ cm}^2/\text{g}$. The $\Delta_{\text{XCOM-MCNP}}$ difference was determined as 5.89%, The $\Delta_{\text{MCNP-EXP.}}$ difference was determined as 6.957% and $\Delta_{\text{XCOM-EXP}}$ difference was determined as 12.44%. These data have been given in Table 4.

In the B-doped ZnO coated thin films, MAC values have been obtained as $0.00138 \pm 0.00029 \text{ cm}^2/\text{g}$ and $0.00267 \pm 0.00034 \text{ cm}^2/\text{g}$ for 0% and 15% B ratio (H. Eskalen et al., 2020). Similarly, in the Sm-doped In_2O_3 coated thin films, Sm ratio have been varied between 0% and 20% and the MAC value increased from $0.00052 \pm 0.00006 \text{ cm}^2/\text{g}$ to $0.00077 \pm 0.000053 \text{ cm}^2/\text{g}$. To gCN study, MAC values were obtained from $0.0144 \pm 0.0361 \text{ cm}^2/\text{g}$ to $0.2150 \pm 0.0641 \text{ cm}^2/\text{g}$ for 0% and 100% Thiourea ratio (Kavun et al., 2023). In the measurements performed via 662 keV gamma for $\text{Al}_{50}\text{B}_{25}\text{Mg}_{25}$ alloy, the MAC value was obtained as $0.1502 \pm 0.008 \text{ cm}^2/\text{g}$ for 0.249 cm alloy thickness and $0.1634 \pm 0.006 \text{ cm}^2/\text{g}$ for 0.516 cm alloy thickness. In the study conducted by Eid S. M. et al., mass attenuation coefficient values were obtained between $0.1242 \text{ cm}^2/\text{g}$ and $0.1379 \text{ cm}^2/\text{g}$ for glass-doped cement mixtures in various proportions (Eid et al., 2022).

The Half Value Layer (HVL), Tenth Value Layer (TVL) and Mean Free Path (MFP) values of $\text{Co}_{20}\text{Cr}_{20}\text{Fe}_{20}\text{Ni}_{20}\text{Si}_{20}$ HEA powders at 662 keV gamma energy. The HVL value was calculated as 3.24 cm for the experimental data, 3.01 cm for the MCNP6.2 and 2.84 cm for the calculations made with XCOM. The TVL value was calculated as 10.76 cm for the experimental data, 10.01 cm for the MCNP6.2 and 9.42 cm for the calculations made with XCOM. Finally, The MFP value was calculated as 4.67 cm for the experimental data, 4.35 cm for the MCNP6.2 and 4.09 cm for the calculations made with XCOM. These obtained data have been given in Table 4.

In the presence of 0% B in B: ZnO coated films, the HVL value was measured as 89.291 cm, the TVL value measured as 296.618 cm and the MFP value measured as 128.82 cm. When 15% B was doped to these films, HVL have been obtained as 55.609 cm, TVL value 184.728 cm and

Table 3
Radiation shielding parameters of $\text{Co}_{20}\text{Cr}_{20}\text{Fe}_{20}\text{Ni}_{20}\text{Si}_{20}$ HEA powders.

Thickness (mm)	I/10		
1.22	0.7225	μ_{exp}	$0.2140 \pm 0.01 \text{ cm}^{-1}$
2.3	0.5745	μ_{MCNP}	0.2300 cm^{-1}
2.9	0.5048	MAC_{exp}	$0.0648 \text{ cm}^2/\text{g}$
3	0.4931	$\text{MAC}_{\text{MCNP6.2}}$	$0.0696 \text{ cm}^2/\text{g}$
3.23	0.4695	MAC_{XCOM}	$0.0740 \text{ cm}^2/\text{g}$
4.14	0.3885	$\Delta_{\text{XCOM-MCNP6.2}}$	5.89%
5	0.3217	$\Delta_{\text{MCNP-EXP.}}$	6.95%
		$\Delta_{\text{XCOM-EXP.}}$	12.44%

Table 4
The Obtained HVL, TVL and MFP data.

	HVL (cm)	TVL (cm)	MFP (cm)
Exp. Data	3.24	10.76	4.67
MCNP6.2	3.01	10.01	4.35
XCOM	2.84	9.42	4.09

MFP value 80.22 cm (H. Eskalen et al., 2020) HVL value of 1.95 cm, TVL value of 6.47 cm and MFP value of 2.81 cm were measured in $\text{Al}_{50}\text{B}_{25}\text{Mg}_{25}$ alloys with similar 662 keV gamma energy value (Yayaşlı et al., 2022). The obtained Radiation shielding parameters of these $\text{Co}_{20}\text{Cr}_{20}\text{Fe}_{20}\text{Ni}_{20}\text{Si}_{20}$ HEA powders have been given in Tables 3 and 4.

4. Conclusion

The CoCrFeNiSi equimolar high entropy alloy was successfully synthesized using the mechanical milling method in this study.

- Form our work research, it can be concluded that the obtained HEA structural characterization after 100 h of milling revealed a solid solution with an FCC structure and a reduction in crystallite size from 23.63 to 3.22 nm.
- The obtained alloy's homogeneity was verified through SEM-EDX results, demonstrating uniform distribution of the five elements in the powder alloy.
- The linear attenuation coefficients (LAC) of the $\text{Co}_{20}\text{Cr}_{20}\text{Fe}_{20}\text{Ni}_{20}\text{Si}_{20}$ HEA powders were investigated, resulting in an LAC value of $0.2140 \pm 0.01 \text{ cm}^{-1}$.
- The experimentally determined mass attenuation coefficient (MAC) value for the $\text{Co}_{20}\text{Cr}_{20}\text{Fe}_{20}\text{Ni}_{20}\text{Si}_{20}$ HEA powders was found to be $0.0648 \text{ cm}^2/\text{g}$.
- Simulation of the experimental system using the $\text{Co}_{20}\text{Cr}_{20}\text{Fe}_{20}\text{Ni}_{20}\text{Si}_{20}$ HEA powder yielded MAC values of 0.0696 and 0.0740 in calculations performed with MCNP6.2 and XCOM, respectively.
- The half-value layer (HVL), tenth-value layer (TVL), and mean free path (MFP) values of the $\text{Co}_{20}\text{Cr}_{20}\text{Fe}_{20}\text{Ni}_{20}\text{Si}_{20}$ HEA powders were determined to be compatible with theoretical calculations, indicating their effective use in radiation shielding.

Declarations

The authors declared that they have no conflicts of interest to this work. We declare that we do not have any commercial or associative interest that represents a conflict of interest in connection with the work submitted.

Ethical approval

Not Applicable.

Declaration of competing interest

The authors declare that they have no known competing financial

interests or personal relationships that could have appeared to influence the work reported in this paper.

Data availability

Data will be made available on request.

Acknowledgments

This work was financially supported by Kahramanmaraş Sutcu Imam University, (KSU) Scientific Research Projects Coordination Department, under Project No. 2019/6–5 YLS, 2020/7–18 M, 2020/7–19 and 2020/7–21 M.

References

- Acikgoz, A., Demircan, G., Yilmaz, D., Aktas, B., Yalcin, S., Yorulmaz, N., 2022. Structural, mechanical, radiation shielding properties and albedo parameters of alumina borate glasses: role of CeO_2 and Er_2O_3 . Mater. Sci. Eng., B 276, 115519. <https://doi.org/10.1016/J.MSEB.2021.115519>.
- Addepalli, S.N., Joladarashi, S., Ramesh, M.R., Arya, S.B., 2022. Effect of mechanical alloying on the microstructure of CoCrNiTiMo high entropy alloy. J. Therm. Spray Technol. 31, 1045–1055. <https://doi.org/10.1007/s11666-021-01317-5>.
- Agar, O., Sayyed, M.I., Akman, F., Tekin, H.O., Kaçal, M.R., 2019. An extensive investigation on gamma ray shielding features of Pd/Ag-based alloys. Nucl. Eng. Technol. 51, 853–859. <https://doi.org/10.1016/j.net.2018.12.014>.
- Alfryyan, N., Alrowaili, Z.A., Somaily, H.H., Olarinoye, I.O., Alwadai, N., Mutuwong, C., Al-Buriachi, M.S., 2022. Comparison of radiation shielding and elastic properties of germinate tellurite glasses with the addition of Ga_2O_3 . J. Taibah Univ. Sci. 16, 183–192.
- ALMisned, G., Sen Baykal, D., Ali, F.T., Bilal, G., Kilic, G., Tekin, H.O., 2023. Gadolinium-tungsten-boron trioxide glasses: a multi-phase research on cross-sections, attenuation coefficients, build-up factors and individual transmission factors using MCNPX. Optik 272, 170216. <https://doi.org/10.1016/J.OPTIK.2022.170216>.
- Almurrayshid, M., Alsagabi, S., Alssalim, Y., Alotaibi, Z., Almsalam, R., 2021. Feasibility of polymer-based composite materials as radiation shield. Radiat. Phys. Chem. 183, 109425 <https://doi.org/10.1016/j.radphyschem.2021.109425>.
- Ashwini, R., Kumar, M.K.P., Rekha, M.Y., Santosh, M.S., Srivastava, C., 2022. Optimization of NiFeCrCo high entropy alloy nanoparticle – graphene (HEA-G) composite for the enhanced electrochemical sensitivity towards urea oxidation. J. Alloys Compd. 903, 163846 <https://doi.org/10.1016/j.jallcom.2022.163846>.
- Cheewasukhanont, W., Limkitjaroenporn, P., Sayyed, M.I., Kothan, S., Kim, H.J., Kaejkhao, J., 2022. High density of tungsten gadolinium borate glasses for radiation shielding material: effect of WO_3 concentration. Radiat. Phys. Chem. 192, 109926.
- Chen, C., Liu, N., Zhou, P., Xiang, H., 2018. Phase stability and mechanical properties of FCC structural $\text{CoCrCu}_0.5\text{FeNi}$ high-entropy alloy with silicon or boron addition. In: Materials Science Forum. Trans Tech Publications Ltd, pp. 169–175. <https://doi.org/10.4028/www.scientific.net/MSF.944.169>.
- Eid, M.S., Bondouk, I.I., Saleh, H.M., Omar, K.M., Sayyed, M.I., El-Khatib, A.M., Elsafi, M., 2022. Implementation of waste silicate glass into composition of ordinary cement for radiation shielding applications. Nucl. Eng. Technol. 54, 1456–1463. <https://doi.org/10.1016/J.NET.2021.10.007>.
- Eskalen, H., Kavun, Y., Kerli, S., Eken, S., 2020. An investigation of radiation shielding properties of boron doped ZnO thin films. Opt. Mater. 105, 109871 <https://doi.org/10.1016/j.optmat.2020.109871>.
- García-Garrido, C., Ferrer, R.S., Salvo, C., García-Domínguez, L., Pérez-Pozo, L., Lloreda-Jurado, P.J., Chicardi, E., 2021. Effect of milling parameters on the development of a nanostructured FCC-TiNb15Mn alloy via high-energy ball milling. Metals 11. <https://doi.org/10.3390/met11081225>.
- Goktas, A., Modanli, S., Tumbul, A., Kilic, A., 2022. Facile synthesis and characterization of ZnO , ZnO:Co , and ZnO/ZnO:Co nano rod-like homojunction thin films: role of crystallite/grain size and microstrain in photocatalytic performance. J. Alloys Compd. 893, 162334 <https://doi.org/10.1016/J.JALLCOM.2021.162334>.
- Gul, A.O., Kavaz, E., Basgoz, O., Guler, O., ALMisned, G., Bahcecii, E., Albayrak, M.G., Tekin, H.O., 2022. Newly synthesized NiCoFeCrW High-Entropy Alloys (HEAs): multiple impacts of B4C additive on structural, mechanical, and nuclear shielding properties. Intermetallics 146, 107593. <https://doi.org/10.1016/j.intermet.2022.107593>.
- Güler, Ö., Şimşek, T., Özkul, İ., Avar, B., Canbay, C.A., Chattopadhyay, A.K., Güler, S.H., 2022. Investigation of shape memory characteristics and production of HfZrTiFeMnSi high entropy alloy by mechanical alloying method. Curr. Appl. Phys. 33, 1–11. <https://doi.org/10.1016/j.cap.2021.10.010>.
- GUO, S., Liu, C.T., 2011. Phase stability in high entropy alloys: formation of solid-solution phase or amorphous phase. Prog. Nat. Sci.: Mater. Int. 21, 433–446. [https://doi.org/10.1016/S1002-0071\(12\)60080-X](https://doi.org/10.1016/S1002-0071(12)60080-X).
- Hu, X., Liu, X., Yan, D., Li, Z., 2022. A high-density non-equiaatomic WTaMoNbV high-entropy alloy: alloying behavior, microstructure and mechanical properties. J. Alloys Compd. 894, 162505 <https://doi.org/10.1016/j.jallcom.2021.162505>.
- Ji, W., Fu, Z., Wang, W., Wang, H., Zhang, J., Wang, Y., Zhang, F., 2014. Mechanical alloying synthesis and spark plasma sintering consolidation of CoCrFeNiAl high-

- entropy alloy. *J. Alloys Compd.* 589, 61–66. <https://doi.org/10.1016/j.jallcom.2013.11.146>.
- Jiang, H., Han, K., Li, D., Cao, Z., 2018. Microstructure and mechanical properties investigation of the CoCrFeNiNb_x high entropy alloy coatings. *Crystals* 8. <https://doi.org/10.3390/crust8110409>.
- Kaewjaeng, S., Wantana, N., Kothon, S., Rajaramakrishna, R., Kim, H.J., Limsuwan, P., Kaewkhaos, J., 2021. Effect of Gd2O3 on the radiation shielding, physical, optical and luminescence behaviors of Gd2O3-La2O3-ZnO-B2O3-Dy2O3 glasses. *Radiat. Phys. Chem.* 185, 109500 <https://doi.org/10.1016/j.radphyschem.2021.109500>.
- Kavun, Y., Eskalen, H., Kerli, S., Kavgaci, M., 2021. Fabrication and characterization of GdxFe2O3(100-x)/PVA (x=0, 5, 10, 20) composite films for radiation shielding. *Appl. Radiat. Isot.* 177, 1–7. <https://doi.org/10.1016/j.apradiso.2021.109918>.
- Kavun, Y., Kerli, S., Eskalen, H., Kavgaci, M., 2022. Characterization and nuclear shielding performance of Sm doped In₂O₃ thin films. *Radiat. Phys. Chem.* 194, 110014 <https://doi.org/10.1016/j.radphyschem.2022.110014>.
- Kavun, Y., Eskalen, H., Kavgaci, M., 2023. A study on gamma radiation shielding performance and characterization of graphitic carbon nitride. *Chem. Phys. Lett.* 811, 140246 <https://doi.org/10.1016/J.CPLETT.2022.140246>.
- Khanna, A., Bhatti, S.S., Singh, K.J., Thind, K.S., 1996. Gamma-ray attenuation coefficients in some heavy metal oxide borate glasses at 662 keV. *Nucl. Instrum. Methods Phys. Res. B* 114, 217–220. [https://doi.org/10.1016/0168-583X\(96\)00196-6](https://doi.org/10.1016/0168-583X(96)00196-6).
- Knoll, G.F., Krane, H.W., 1981. Radiation detection and measurement. *Proc. IEEE*. <https://doi.org/10.1109/PROC.1981.12016>.
- Krane, K.S., Lynch, W.G., 1989. Introductory nuclear physics. *Phys. Today*. <https://doi.org/10.1063/1.2810884>.
- Kumar, D., Maulik, O., Bagri, A.S., Prasad, Y.V.S.S., Kumar, V., 2016. Microstructure and characterization of mechanically alloyed equiatomic AlCuCrFeMnW high entropy alloy. *Mater. Today Proc.* 3, 2926–2933. <https://doi.org/10.1016/j.matpr.2016.09.005>.
- Kumar, A., Mucalo, M., Bolzoni, L., Li, Y., Kong, F., Yang, F., 2022a. Fabrication, microstructure, mechanical, and electrochemical properties of NiMnFeCu high entropy alloy from elemental powders. *Metals*. <https://doi.org/10.3390/met12010167>.
- Kumar, A., Mucalo, M., Bolzoni, L., Li, Y., Kong, F., Yang, F., 2022b. Fabrication, microstructure, mechanical, and electrochemical properties of NiMnFeCu high entropy alloy from elemental powders. *Metals* 12. <https://doi.org/10.3390/met12010167>.
- Kursun, C., Gögebakan, M., Eskalen, H., 2018. Mechanical properties, microstructural and thermal evolution of Mg 65 Ni 20 Y 15–x Six (X = 1, 2, 3) alloys by mechanical alloying. *Mater. Res. Express* 5, 036512. <https://doi.org/10.1088/2053-1591/ab4050>.
- Liu, X., Zhang, L., Xu, Y., 2017. Microstructure and mechanical properties of graphene reinforced Fe50Mn30Co10Cr10 high-entropy alloy composites synthesized by MA and SPS. *Appl. Phys. Mater. Sci. Process* 123, 1–7. <https://doi.org/10.1007/S00339-017-1151-7/TABLES/2>.
- Liu, H., Xin, C., Liu, L., Zhuang, C., 2021. Effects of different contents of each component on the structural stability and mechanical properties of co-cr-fe-ni high-entropy alloys. *Appl. Sci.* 11 [https://doi.org/11062832](https://doi.org/10.3390/app11062832).
- Ma, H., Shek, C.H., 2020. Effects of Hf on the microstructure and mechanical properties of CoCrFeNi high entropy alloy. *J. Alloys Compd.* 827 <https://doi.org/10.1016/j.jallcom.2020.154159>.
- Mahmoud, K.A., Sayyed, M.I., Tashlykov, O.L., 2019. Comparative studies between the shielding parameters of concretes with different additive aggregates using MCNP-5 simulation code. *Radiat. Phys. Chem.* 165, 108426 <https://doi.org/10.1016/J.RADPHYSCHM.2019.108426>.
- Miedema, A.R., De Chatel, P.F., De Boer, F.R., 1980. Cohesion in alloys—fundamentals of a semi-empirical model. *Phys. B+C* 100, 1–28.
- Moschetti, M., Burr, P.A., Obbard, E., Krusic, J.J., Hosemann, P., Gludovatz, B., 2022. Design considerations for high entropy alloys in advanced nuclear applications. *J. Nucl. Mater.* 567, 153814 <https://doi.org/10.1016/j.jinucmat.2022.153814>.
- Nagarjuna, C., Song, J., Jeong, K.Y., Pin, M.-W., Song, G., Lee, J.K., Na, Y.-S., Kim, H.S., Kim, K.B., Hong, S.-J., 2022. Developing harmonic structure in CoCrFeMnNi high entropy alloy to enhance mechanical properties via powder metallurgy approach. *J. Mater. Res. Technol.* 17, 1686–1695. <https://doi.org/10.1016/j.jmrt.2022.01.098>.
- Prasad, A., John, M.S., John, F., 2023. Facile auto-combustion synthesis of nanocrystalline BaCoFe6O11-Structural and Optical properties. *Mater. Today Proc.* <https://doi.org/10.1016/J.MATPR.2023.05.403>.
- Shivam, V., Sanjana, V., Mukhopadhyay, N.K., 2020. Phase evolution and thermal stability of mechanically alloyed AlCrFeCoNiZn high-entropy alloy. *Trans. Indian Inst. Met.* 73, 821–830. <https://doi.org/10.1007/S12666-020-01892-1/TABLES/3>.
- Shkodich, N.F., Kovalev, I.D., Kuskov, K.V., Kovalev, D.Yu., Vergunova, Yu.S., Scheck, Yu.B., Vadchenko, S.G., Politano, O., Baras, F., Rogachev, A.S., 2022. Fast mechanical synthesis, structure evolution, and thermal stability of nanostructured CoCrFeNiCu high entropy alloy. *J. Alloys Compd.* 893, 161839 <https://doi.org/10.1016/j.jallcom.2021.161839>.
- Singh, A.K., Subramaniam, A., 2012. Thermodynamic rationalization of the microstructures of CrFeNi & CuCrFeNi alloys. In: *Advanced Materials Research*, pp. 3–7. <https://doi.org/10.4028/www.scientific.net/AMR.585.3>.
- Suryanarayana, C., 2001. Mechanical alloying and milling. *Prog. Mater. Sci.* 46, 1–184. [https://doi.org/10.1016/S0079-6425\(99\)00010-9](https://doi.org/10.1016/S0079-6425(99)00010-9).
- Taghvaei, A.H., Khoshrodi, A.M., 2018. Characterization, thermodynamic analysis and magnetic investigation of new soft magnetic amorphous/nanocrystalline Co50Fe21Ti19Ta5B5 powders produced by mechanical alloying. *J. Alloys Compd.* 742, 887–896. <https://doi.org/10.1016/j.jallcom.2018.01.382>.
- Toroghinejad, M.R., Pirmoradian, H., Shabani, A., 2022. Synthesis of FeCrCoNiCu high entropy alloy through mechanical alloying and spark plasma sintering processes. *Mater. Chem. Phys.* 212, 126433 <https://doi.org/10.1016/j.matchemphys.2022.126433>.
- Wang, X., Xie, H., Jia, L., Lu, Z., 2012. Effect of Ti, Al and Cu addition on structural evolution and phase constitution of FeCoNi system equimolar alloys. In: *Materials Science Forum*, Trans Tech Publications Ltd, pp. 335–338. <https://doi.org/10.4028/www.scientific.net/MSF.724.335>.
- Wang, Kaizhuo, Hu, J., Chen, T., Zhang, W., Fan, H., Feng, Y., Zhao, Z., Wang, Kaijun, 2021. Flexible low-melting point radiation shielding materials: soft elastomers with GaInSnPbBi high-entropy alloy inclusions. *Macromol. Mater. Eng.* 306, 1–10. <https://doi.org/10.1002/mame.202100457>.
- Wu, S., kai, Pan, Y., Wang, N., Lu, T., Dai, W., ji, 2019. Azo dye degradation behavior of AlFeMnTiM (M = Cr, Co, Ni) high-entropy alloys. *Int. J. Miner. Metall. Mater.* 26, 124–132. <https://doi.org/10.1007/s12613-019-1716-x>.
- Wu, H., Zhang, S., Wang, Z.Y., Zhang, C.H., Chen, H.T., Chen, J., 2022. New studies on wear and corrosion behavior of laser cladding FeNiCoCrMox high entropy alloy coating: the role of Mo. *Int. J. Refract. Metals Hard Mater.* 102 <https://doi.org/10.1016/j.ijrmhm.2021.105721>.
- Xu, X.D., Guo, S., Nieh, T.G., Liu, C.T., Hirata, A., Chen, M.W., 2019. Effects of mixing enthalpy and cooling rate on phase formation of AlxCrCoFeNi high-entropy alloys. *Materialia (Oxf)* 6. <https://doi.org/10.1016/j.mtla.2019.100292>.
- Yaykaşlı, H., Gögebakan, M., 2022. Microstructural, thermal, and radiation shielding properties of Al50B25Mg25 alloy prepared by mechanical alloying. *J. Mater. Sci. Mater. Electron.* 33, 2350–2359. <https://doi.org/10.1007/S10854-021-07434-9/TABLES/2>.
- Yeh, J.W., Chen, S.K., Lin, S.J., Gan, J.Y., Chin, T.S., Shun, T.T., Tsau, C.H., Chang, S.Y., 2004. Nanostructured high-entropy alloys with multiple principal elements: novel alloy design concepts and outcomes. *Adv. Eng. Mater.* 6, 299–303. <https://doi.org/10.1002/adem.200300567>.
- Zhang, C., Wu, G.F., Dai, P.Q., 2015. Phase transformation and aging behavior of Al0.5CoCrFeNiSi0.2 high-entropy alloy. *J. Mater. Eng. Perform.* 24, 1918–1925. <https://doi.org/10.1007/s11665-015-1475-4>.
- Zhang, L.J., Zhang, M.D., Zhou, Z., Fan, J.T., Cui, P., Yu, P.F., Jing, Q., Ma, M.Z., Liaw, P.K., Li, G., Liu, R.P., 2018. Effects of rare-earth element, Y, additions on the microstructure and mechanical properties of CoCrFeNi high entropy alloy. *Mater. Sci. Eng.* 725, 437–446. <https://doi.org/10.1016/j.mse.2018.04.058>.
- Zhang, J., Ren, B., Zhao, R., Liu, Z., Cai, B., Zhang, G., 2021. Effect of Co on the microstructure and oxidation behavior of CoxCrCuFeMnNi high entropy alloy powders. *Micron* 142. <https://doi.org/10.1016/j.micron.2020.102995>.
- Zhang, P., Li, Z., Liu, H., Zhang, Y., Li, H., Shi, C., Liu, P., Yan, D., 2022. Recent progress on the microstructure and properties of high entropy alloy coatings prepared by laser processing technology: a review. *J. Manuf. Process.* 76, 397–411. <https://doi.org/10.1016/j.jmapro.2022.02.006>.
- Zuo, T.T., Li, R.B., Ren, X.J., Zhang, Y., 2014. Effects of Al and Si addition on the structure and properties of CoFeNi equal atomic ratio alloy. *J. Magn. Magn. Mater.* 371, 60–68. <https://doi.org/10.1016/j.jmmm.2014.07.023>.